Detection of weak gravitational lensing distortions of distant galaxies by cosmic dark matter at large scales

David M. Wittman*, J. Anthony Tyson, David Kirkman, Ian Dell'Antonio† & Gary Bernstein‡

* *Bell Laboratories, Lucent Technologies, Murray Hill, New Jersey, 07574, USA*
† *Kitt Peak National Observatory, NOAO, Tucson, Arizona 85726, USA*
‡ *Astronomy Department, University of Michigan, Ann Arbor, Michigan 48109, USA*

Most of the matter in the Universe is not luminous, and can be observed only through its gravitational influence on the appearance of luminous matter. Weak gravitational lensing is a technique that uses the distortions of the images of distant galaxies as a tracer of dark matter: such distortions are induced as the light passes through large-scale distributions of dark matter in the foreground. The patterns of the induced distortions reflect the density of mass along the line of sight and its distribution, and the resulting 'cosmic shear' can be used to distinguish between alternative cosmologies. But previous attempts to measure this effect have been inconclusive. Here we report the detection of cosmic shear on angular scales of up to half a degree using 145,000 galaxies and along three separate lines of sight. We find that the dark matter is distributed in a manner consistent with either an open universe, or a flat universe that is dominated by a cosmological constant. Our results are inconsistent with the standard cold-dark-matter model.

The large-scale distribution of dark matter depends both upon the nature of the dark matter and the global cosmological parameters that describe the Universe. Information on the large-scale distribution of matter is thus one of the primary goals of modern observational astronomy. To date, most of what we know about the large-scale structure of the Universe comes from the observed anisotropies in the cosmic microwave background (CMB) and from the distribution of galaxies. The CMB provides the earliest sample of mass fluctuations, from a time when the Universe was 100,000 times younger[1]. Different cosmological models predict different scenarios in the growth of mass structures over cosmic time, so comparison of the CMB-derived mass spectrum with that seen at later times is a powerful test of cosmological models. The large-scale mass distribution at later times has traditionally been characterized through the large-scale distribution of galaxies on the assumption that light traces mass.

The distribution of this dark mass can be investigated more directly via its gravitational effects on the appearance of background galaxies. Any foreground mass bends light rays from a distant source, moving the apparent position of the source to a new position on the sky and stretching its image tangentially, by an amount proportional to the foreground mass. This weak lensing effect has already been used to study the mass distribution within clusters of galaxies, where the large mass associated with the clusters makes the gravitationally induced ellipticity of the background galaxies easily detectable[2–7]. In principle, weak lensing can also tell us about large-scale structure through the cumulative effect of many intervening overdensities. A deep image of a patch of the sky looks out through the three-dimensional arrangement of galaxies seen in projection: any two galaxies are not likely to be physical neighbours and in the absence of lensing, their projected shapes or ellipticities are statistically uncorrelated. In the presence of foreground mass overdensities—that is, those occurring between distant galaxies and the observer—the light rays from galaxies narrowly separated on the sky travel similar paths past intervening mass concentrations and thus undergo similar image distortions. The resulting correlation of distant galaxy ellipticities is highest at small angular separation and drops for widely separated galaxies whose light bundles travel through completely different structures (Fig. 1). Different cosmological models predict different behaviour for correlations of galaxy ellipticites versus angular separation on the sky.

Theoretical expectations for this cosmic shear on angular scales of 10–30 arcmin range from a few per cent for the standard cold-dark-matter model to less than one per cent for an open universe which would expand forever[8–15]. The typical background galaxy has an
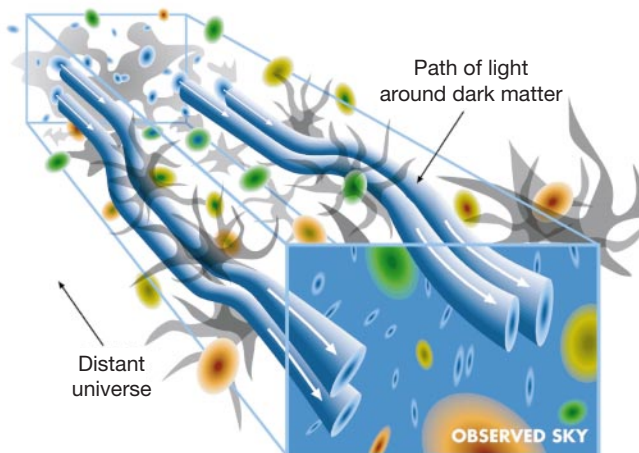

Figure 1 The distorted universe. Light rays from distant galaxies travel a tortuous path through a universe filled with clustering dark mass. Every bend in the path of a bundle of light from a distant galaxy stretches its apparent image. The orientation of the resulting elliptical images of galaxies contains information on the size and mass of the gravitational lenses distributed over the light path. The figure shows a schematic view of weak gravitational lensing by large-scale mass structure: distant galaxy orientation is correlated on scales characteristic of the lensing dark matter structures. Light bundles from two distant galaxies which are projected closely together on the sky follow similar paths and undergo similar gravitational deflections by intervening dark matter concentrations. Apparent orientations of distant galaxies are thus correlated on angular scales of less than a few degrees. The larger the mass in the gravitational deflectors, the larger the faint galaxy ellipticity correlations on a given angular scale. These ellipticity correlations of distant galaxies reveal the statistics of the large-scale dark matter distribution in the intervening universe—a central diagnostic of the underlying cosmology.

 143

intrinsic ellipticity of roughly 30%, so that many thousands of source galaxies must be averaged together to detect the small change induced by cosmic shear. In addition, a large area of sky must be covered, because mass structures should span a few arcminutes to a degree at a typical mid-path distance of redshift 0.4 (about three billion light years). Earlier attempts to measure cosmic shear were inconclusive[16–19], with the main difficulty being control of systematic errors in galaxy shapes arising from the optical system or the process of observation. The earliest attempts with photographic plates, while covering a large field, suffered from plate-to-plate systematics as well as nonlinearity and lack of sensitivity. The sensitivity, linearity and reproducibility problems were solved with the advent of charge-coupled devices (CCDs), but the small field size covered by early CCDs was a problem. Mosaics of large CCDs now approach the desired one-degree field size, and are stimulating much activity in weak gravitational lensing.

We have imaged large areas of sky in several directions using a mosaic of CCDs on a large telescope, covering hundreds of thousands of distant galaxies at multiple wavelengths. We describe the steps taken to minimize systematic errors and to select 145,000 of the most reliable distant galaxy measurements. We find significant ellipticity correlations on angular scales of 0.04°–0.5°. This is, to our knowledge, the first direct probe of the aggregate mass distribution in the Universe at late times on the scale of several billion light years, and the results are consistent with two leading cosmological models.

Wide-field imaging with control of systematic shape errors

We observed three blank (that is, not containing any known mass concentrations) fields—at 23 h 48 min, +00° 57′ J2000; 04 h 29 min, −36° 18′; and 11 h 38 min, −12° 33′—over a period of several years.

This was done using the Big Throughout Camera[20], which comprises an array of four large, blue-sensitive CCDs at the Cerro Tololo Inter-American Observatory's 4-m Blanco telescope. Constructed originally for weak lens observations, this camera covers a 35-arcmin field of view with 0.43-arcsec pixels. We took multiple 500-s exposures shifted by 5–7 arcmin and combined them to cover a 43-arcmin field. Before combining, we took several steps to reduce systematic errors arising from the optical system. First, we registered all the images onto a common linear coordinate system, free of the known radial distortion of the telescope optics. We then used the shapes of stars, which are foreground point sources free of the gravitational lensing effect, to correct any additional anisotropies in the point-spread function (the response of the optical system to point sources), such as those due to astigmatism and guiding errors.

The shape of a star or galaxy can be described by its second central moments, $I_{xx} \equiv \Sigma I w x^2$, $I_{yy} \equiv \Sigma I w y^2$ and $I_{xy} \equiv \Sigma I w x y$, where $I(x,y)$ is the intensity distribution above the night sky level, $w(x,y)$ is a weight function, the sum is over a contiguous set of pixels defined as belonging to the galaxy, and the coordinate system has been translated so that the first moments vanish. The second moments can be combined to form a size, $I_{xx} + I_{yy}$, and two components of a pseudo-vector ellipticity, $e_1 \equiv (I_{xx} - I_{yy})/(I_{xx} + I_{yy})$ and $e_2 \equiv 2I_{xy}/(I_{xx} + I_{yy})$, which vary in the range $[-1,1]$ (ellipticity in its colloquial sense is the amplitude of this pseudo-vector, $\epsilon \equiv (e_1^2 + e_2^2)^{1/2}$ with its range $[0,1]$). Traditional intensity-weighted moments are calculated with $w = 1$, but this produces ellipticity measurements with noise properties that are far from optimal—or even divergent. In cases of white noise, the formal optimal weight for an elliptical source is a noise-free image of that elliptical source[21].
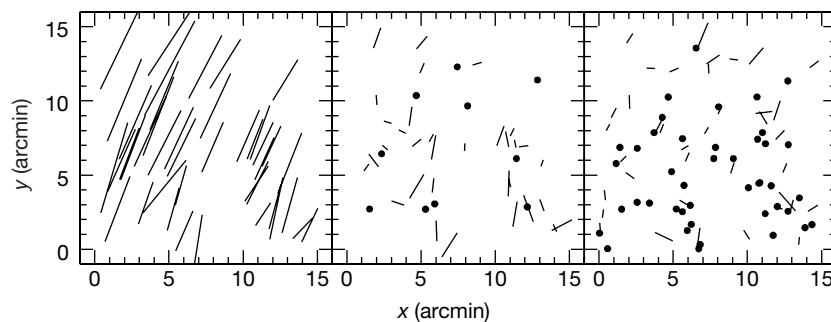

Figure 2 Making stars round. Foreground stars at many positions in the field of view are used to correct for position-dependent systematic ellipticity error. Convolution with a position-dependent kernel with ellipticity components equal and opposite to those of the stars reduces this systematic error everywhere in the field. Here we illustrate this technique with one particularly bad frame of raw data from one of the four CCDs in our mosaic. Each panel represents stars at their positions in the field as a line encoding the ellipticity and position angle, or as a point if the ellipticity is less than one per cent. The left panel is the raw data; the stars in a more typical frame have only half the ellipticity of those shown here, or about 5%. The middle panel shows the stellar shapes in the same single image after convolution with the rounding kernel. The stars are vastly less out of round, but local correlations still exist. The right panel shows the final shapes of stars in the same region of sky, after combining ten shifted exposures, convolving the combined image, and measuring the shapes in more than one filter. Many of the local correlations in the middle panel have disappeared. The density of stars is greater due to better identification of stars in the combined image. The final field size is roughly ten times larger in area than this patch, and contains about 1,000 such stars in most of our mid-latitude fields. This figure is for illustration purposes only; Fig. 4 contains a quantitative assessment of the final level of systematic error.

Table 1 Summary of cosmological models

Model*	Ω_b	$\Omega_{matter} - \Omega_b$	Ω_Λ	H_0	n	σ_8	Normalization
Standard cold dark matter (blue)	0.05	0.95	0	50	1.0	1.17	COBE only
Λ-dominated, flat (green)	0.039	0.291	0.67	70	0.94	0.84	COBE + clusters
Open universe (orange)	0.045	0.405	0	65	1.01	0.71	COBE + clusters

These cosmological models were chosen in order to put our ellipticity correlation measurements in context. The old standard cold-dark-matter model, in which the Universe is nearly closed by cold dark matter, is also disfavoured in other observations. Its r.m.s. mass contrast is normalized to that found 300,000 years after the Big Bang via the cosmic microwave background radiation fluctuations observed with the Cosmic Background Explorer satellite (COBE). The other two models agree with a wide variety of observations, but only the Λ-dominated, (flat) model also agrees with the recent evidence from supernova studies for accelerated expansion. Ω_b is the fraction of critical density in ordinary (baryonic) matter. Ω_{matter} is the fraction in all matter (mostly dark matter), and Ω_Λ is the fraction in dark energy (the cosmological constant). H_0 is the Hubble constant in units of km s^{-1} Mpc^{-1}. The power spectrum $P(k)$ of mass density fluctuations is often plotted in terms of inverse size: the wavenumber k is inversely proportional to length. The parameter n is the slope of the primaeval density power spectrum as a function of k: $P(k) \propto k^n$. For a scale-free power spectrum of density fluctuations, $n = 1$. The parameter σ_8 is the current r.m.s. mass contrast in a random sphere of radius $8(100/H_0)$ Mpc compared with that for numbers of galaxies[36]. The choice of $n = 1$ and COBE normalization for standard cold dark matter results in too much mass fluctuation on galaxy cluster scales. By adjusting the slope n and current r.m.s. mass contrast σ_8, models can be forced to fit the r.m.s. mass contrast now on galaxy cluster scales as well as the COBE normalization.

* Colour in parentheses refers to the corresponding line in Fig. 5.

In the absence of such an image, weak lensing measurements are generally made with circular gaussian weights. We use an elliptical gaussian as the weight function, which places more weight on the inner parts of the galaxy image where the signal-to-noise ratio is higher, and is nearly optimal for most point-spread functions and for typical exponential galaxy profiles.

The moments of the gaussian weight ellipse are iterated (from initial values provided by unweighted moments) to match the size and shape of the object, in order to obtain the highest possible signal-to-noise ratio and to ensure that the measured ellipticity is not biased toward the shape of the weight function. This technique of adaptively weighted moments has been extensively tested on simulated and real data, and has been shown to be unbiased. On simulated data, the algorithm recovers a somewhat higher fraction of the artificially induced shear than does simple intensity weighting. However, our final results do not depend on this particular weighting scheme. Its real benefit lies in rejection of peculiar objects, the vast majority of which are overlapping galaxies seen in projection. If the final centroid of a galaxy differs significantly from the starting centroid, that galaxy is rejected. If the centroid does not shift, the galaxy is accepted (and probably suffers little contamination by its neighbour). Object candidates are also rejected if: the centroid or the ellipticity fails to converge; they are too near the edge of the image; the size grows too large; or the moments are negative. About one-third of candidates found by the detection software (which provides the initial unweighted moments and can 'detect' occasional noise peaks) are rejected. For candidates which survive, the measurement error in the final ellipticity is accurately estimated by propagating the poissonian photon noise through the moment equations.

We used foreground stars at many positions in the field of view to measure and correct for systematic ellipticity error. Stars are distingui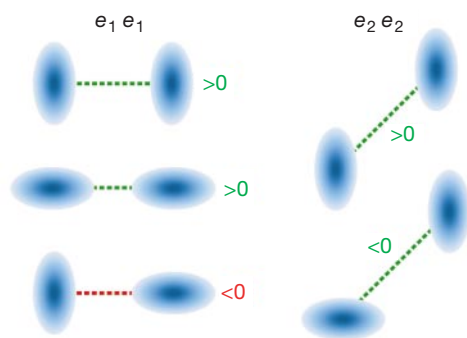shed from galaxies by their clear separation at the bright end of a size/flux-density diagram. We identified roughly 100 such stars on each exposure of each CCD and made a least-squares fit (with 3σ cut-off) of a second-order polynomial to the spatial variation of their ellipticity components $e_1^\star(x,y)$ and $e_2^\star(x,y)$, which would be zero at all points in an ideal observation free of point-spread function anisotropy. Fischer and Tyson[22] have shown that non-zero $e_1^\star$ and $e_2^\star$ can be cancelled by convolution with a small (three pixel square) flux-conserving kernel with ellipticity components equal and opposite to those of the stars. Simulations as well as weak lensing data on clusters of galaxies show that systematics induced in faint galaxies are also removed in this process of circularizing stars. We convolved each image with its resulting position-dependent circularizing kernel, after which the stellar ellipticities show little variation as a function of position. We then combined the images by averaging with a 3σ cut-off, and repeated the point-spread function rounding on the combined image (using roughly 1,000 stars and a fourth-order polynomial in this case). Figure 2 depicts the evolution of one of our worst raw images through this process.

Catalogues of distant galaxies

We repeated the observing and image processing for each field in three wavelength bands centred on 450 nm, 650 nm and 850 nm (ref. 23), and for two of the fields we also took 550-nm images. The mean exposure time at each wavelength was 3,400 s. In each field, we used standard software[24] to identify object positions and fluxes on the 650-nm image (which is the deepest image in each field), yielding roughly 150,000 objects per field. We have confirmed the robustness of the weighted intensity moments in our detected object catalogues by using different (FOCAS[25] with adaptive circular kernel[26]) detection and evaluation software. At the position of each object, we evaluated the weighted moments at each wavelength, retaining only the measurements which the iterative weighted-moment algorithm did not flag as suspect. Measurements with small sizes ($I_{xx} < 1.0$ or $I_{yy} < 1.0$) were also excluded as suspect. The result is a list of multiple independent ellipticity measurements (and corresponding estimated measurement errors σ_i) for each object.

We then computed the best estimate of each galaxy's ellipticity by averaging the remaining measurements, weighted inversely by their estimated errors. If either of the ellipticity components at any wavelength deviated from this mean by more than $3\sigma_i$, that wavelength was eliminated and the process repeated. This step thus eliminates individual galaxy ellipticity measurements at wavelengths at which objects were noisy or blended, and it also reduces the systematic errors because the images at different wavelengths do not share the same residual point-spread function anisotropy. Finally we rejected objects with $\epsilon > 0.6$ as likely to be blends of more than one object, and applied flux density criteria (1.8 μJy $> F_\nu > 0.11$ μJy through the 650-nm filter, 23–26 R-band magnitude) to select objects likely to be distant galaxies. We use these same selection criteria in calibrating the typical redshift of the background galaxies (below). The final catalogues contain about 45,000 galaxies in each field. A visual inspection of the final catalogues indicates that they are free of spurious objects such as bits of scattered light around bright stars.

These observed ellipticities must be corrected for the overall broadening effect of the point-spread function, which makes galaxies with elliptical profile appear more circular even if the point-spread function itself is perfectly isotropic. To calibrate this effect, we took a deep image with a very small point spread (the Hubble Deep Field South) and convolved it to the resolution of our final images, which is 1.07–1.25 arcsec as measured by the full-width at half-maximum at 650 nm. (The resolution on individual exposures, or "seeing", was better, but the stellar size is larger in the final image with systematic shape errors removed from the point-spread function.) While some isolated galaxies became broader and less elliptical as predicted, most merged with their neighbours,

Figure 3 Lens-induced galaxy orientation correlations. Pairs of background galaxies, separated on the sky by some angle, can have their relative orientations affected by weak lensing. The ellipticity components of any galaxy i with respect to galaxy j can be visualized as $e_1 = \epsilon \cos(2\theta)$ and $e_2 = \epsilon \sin(2\theta)$, where ϵ is the scalar ellipticity and θ is the position angle with respect to a line joining the two galaxies. Ellipticity correlation functions are computed from the products of the ellipticity components of millions of such pairs, as a function of angular separation between pairs. A variety of relative orientations are illustrated along with their contributions to the correlations. Gravitational lensing leaves its signature on these correlations in several ways. First, the amplitude of the correlations scales with the amount of foreground mass. Second, the correlations are large at small separations and drop to nearly zero at large separations in a particular way. The bottom (red) case on the left cannot be caused by gravitational lensing, so that $\langle e_1 e_1 \rangle$ (averaged over many pairs) is always positive in the absence of systematic error. But lensing can cause the e_2 product to have either sign, as shown, and $\langle e_2 e_2 \rangle$ should become negative at a separation characteristic of the underlying cosmology. Third, correlations between e_1 and e_2 (not shown here) are not induced by gravitational lensing, so that any putative measurement of a weak lensing effect should vanish in the cross-correlation $\langle e_1 e_2 \rangle + \langle e_2 e_1 \rangle$.

producing many more elliptical objects than predicted and preventing the construction of a clear relationship between observed and true ellipticity for individual galaxies.

Instead of constructing such a relationship we calibrated the fraction of cosmic shear recovered, as a function of resolution, from the ensemble of galaxies matching our selection criteria. We induced a known shear into the Hubble Deep Field South, convolved to the desired resolution, applied the same galaxy measurement and selection routines (at 650 nm only), and measured the mean ellipticity of the resulting sample. We averaged over repeated shears in several different directions to assess the measurement errors. The ratio of induced to recovered ellipticity was 4.5 ± 0.5, with no clear trend as a function of resolution. The lack of such a trend would be quite surprising for isolated galaxies, but the coalescence of galaxy images appears to be the dominant effect. In the fairly small range of 1.07–1.25-arcsec resolution, this effect does not change the recovery factor by more than the measurement error of 0.5, so we adopt 4.5 as an overall ellipticity recovery factor.

Ellipticity correlations of distant galaxies

Two physically revealing ellipticity correlation functions have been defined[10]. In this approach, the ellipticity components of a galaxy i are calculated not with respect to the arbitrary x and y axes of the image, but with respect to the line joining it to another galaxy j (Fig. 3). Averaging over all galaxies i and j separated by angle θ on the sky, the correlations $\xi_1(\theta) \equiv \langle e_{1i}e_{1j} \rangle$ and $\xi_2(\theta) \equiv \langle e_{2i}e_{2j} \rangle$ have a unique signature in the presence of gravitational lensing, explained in detail in Fig. 3 legend. We recently reported the detection of a cosmic shear signal in the quadrature sum of these correlation functions[27].

Figure 4 shows the ellipticity correlations for each of the three fields in the angular separation range 2–36 arcmin (top panels). The plotted errors indicate 68% confidence intervals determined from 200 realizations (bootstrap-resampled) of the final galaxy catalogue in each field. Note that the measurements in different angular separation bins are not statistically independent, but ξ_1 and ξ_2 are independent from each other, as are the three fields. At $\theta = 6.1$ arcmin, the confidence that $\xi_1 > 0$ is 97%, 99.5% and 99.5% for the three fields in the order shown in Fig. 4. Similarly, the confidence that $\xi_2 > 0$ at the same angular scale is 87.5%, >99.5% and 97% respectively. Some cosmic variance, that is, real systematic differences among fields of this size is expected[28], but the statistical errors are too large to examine this effect. We plot the average over the three fields in the lower panels of Fig. 4, with 1σ errors in the mean derived from the variance among the fields (black points and errors). The signature of gravitational lensing by large-scale structure is evident: ξ_1 declines as the angular scale increases, but is positive at all scales, while ξ_2 matches ξ_1 at small scales but drops below zero at large scales. This result is robust. Similar, but lower signal-to-noise, profiles are obtained if we use unweighted moments or moments from the 650-nm images only.

We performed several tests for systematic errors. The effects of residual point-spread function anisotropy are demonstrated by plotting the correlation functions of the stars (blue in Fig. 4). These are far closer to zero than are the galaxy correlations. Only ξ_1 in the innermost bin has an apparently significant stellar correlation. To test the effect that this might have on the galaxy correlations, we computed the star–galaxy correlations $\langle e_{1,star}e_{1,gal} \rangle$ and $\langle e_{2,star}e_{2,gal} \rangle$ (green in Fig. 4). The star–galaxy correlations are extremely close to zero in this bin. There are also tests involving the galaxy sample alone. The cross-correlation $\xi_3 \equiv \frac{1}{2}(\langle e_{1i}e_{2j} \rangle + \langle e_{2i}e_{1j} \rangle)$ should vanish in the absence of systematic errors (red in Fig. 4). The result is reassuringly close to zero. The plotted errors for ξ_3 can also
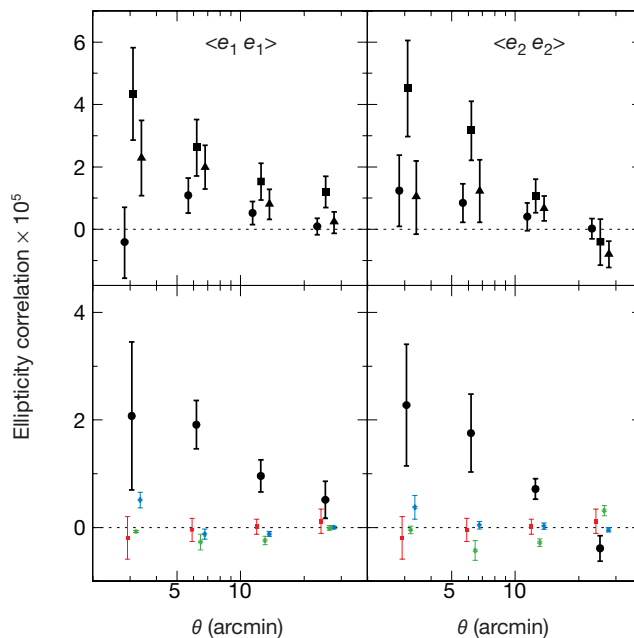

Figure 4 Detection of ellipticity correlations. The upper panels show the measured ellipticity correlations as a function of angle for three independent fields covering a total of 1.5 square degrees (ξ_1 at left and ξ_2 at right). Markers have been slightly offset horizontally for clarity. From left to right in each bin are fields at 11 h 38 min, −12° 33′, 23 h 48 min, +00° 57′, and 04 h 29′, −36° 18′ (J2000). In each field, roughly 45,000 faint galaxies passed all the filters and significance tests, from an initial catalogue of about 150,000 objects. Errors shown are 68% confidence intervals determined from 200 bootstrap-resamplings of the galaxy catalogues. The lower panels show the mean of the ellipticity correlation functions over the three fields (black), with 1σ errors derived from the variance between fields. The behaviour as a function of angle matches that expected from weak gravitational lensing by large-scale structure. The lower panels also contain several null tests of systematic error. The cross-correlation of the galaxies ξ_3 should vanish in the absence of systematic error, and in fact is everywhere consistent with zero (red). The ellipticity correlations of stars (blue) are everywhere consistent with zero except in the innermost bin of ξ_1. The effect of non-zero stellar correlations on the galaxy correlations is illustrated by the star–galaxy correlation (green), which is very close to zero in this bin. An additional test of systematics, a search for preferential alignment of galaxies with the CCD axes, is also null. Though galaxy ellipticity correlations continue to rise at smaller angles, the smaller number of galaxy pairs makes the measurement noisier, there are few closely-spaced stars to assess systematic error, and the theoretical interpretation on small scales is difficult.

be taken as an indicator of the statistical error associated with the number and distribution of galaxies included in the catalogues (but reduced due to the averaging of two functions in ξ_3). This estimate of statistical error agrees roughly with that shown for ξ_1 and ξ_2. Finally, the weak lensing signature disappears if we randomize the galaxy positions.

Apart from these null tests, there are also affirmative tests. One test is to take similar data centred on a cluster of galaxies of known mass. A 650-nm image of massive cluster at redshift 0.45, taken with the same camera and processed in the same way, exhibits correlation functions (ξ_1 and ξ_2) of the expected angular dependence and of larger amplitude than in any of the three blank fields, despite likely contamination of the galaxy sample by cluster members. ξ_3 also vanishes in this field. Another test involves inverting the back-

Figure 5 Comparison of ellipticity correlations with predictions. We plot our measurements of ellipticity correlations with 1σ errors on a logarithmic scale along with theoretical predictions based on various models for a cold-dark-matter universe. The top panel shows ξ_1, the middle panel shows $\xi_2 > 0$, and the lower panel shows $\xi_2 < 0$. In each panel, the blue theoretical curve is for the standard cold dark matter model, the solid green curve is for a universe with a cosmological constant (ΛCDM), and the orange curve is for an open universe; detailed parameters are given in Table 1. The dotted green curve shows the effect of decreasing the mode of the background galaxy redshift distribution, $2z_0$, from 1.0 to 0.6 for one model (ΛCDM). The errors shown are derived from the variance among three fields. The data from Fig. 4 have been multiplied by a correction factor of 20 here, to compensate for the ellipticity dilution factor of 4.5 described in the text, which is squared in the correlation functions. The measurements are consistent with ΛCDM and an open universe at the 3σ level despite the visual impression given by ξ_2, which is due to the logarithmic axes. Standard cold dark matter is inconsistent with ξ_1 at many sigma. This measurement of ellipticity correlations due to cosmic shear over half-degree angular scales is in agreement with a variety of other evidence in ruling out standard cold dark matter. Weak lens observations of larger fields and more distant galaxies will be able to clearly distinguish between the remaining models, or suggest the need for a new model.

ground galaxy ellipticity distribution to yield a map of projected mass in each blank field. We find occasional mass concentrations which can often be identified with likely foreground clusters, but no linear features or pile-ups at the edges of the image which might indicate problems in the background galaxy catalogues. Furthermore, when mass is mapped using only those galaxies likely to be behind a serendipitous cluster (on the basis of colour information), the lensing signal from that cluster increases markedly. This corroborates the idea that the correlation functions are accumulating over many sources and many overdensities spread throughout the line of sight. All these tests indicate that we have indeed measured cosmic shear in our blank fields and that contamination from surviving systematic error is low. We now turn to comparisons with theoretical predictions of this effect.

Comparison with theoretical predictions

Correlations between the ellipticity of galaxies increase strongly with background galaxy redshift, so we must first constrain the source redshift distribution, $N(z)$. Very little is known about the redshift distribution of galaxies as faint as those used here, so we assume a simple model where $N(z) \propto z^2 \exp(-z/z_0)$, and adjust z_0 to match weak gravitational lensing observations of a high-redshift galaxy cluster of known velocity dispersion (MS1054 at $z = 0.83$)[29]. We observed this cluster with the same camera and telescope and reduced the data in the same way as for the blank fields, and compared the faint galaxy ellipticities (tangential to the cluster centre) to that expected for a range of z_0. We found that $z_0 = 0.5$ was the best match.

This model of $N(z)$ was used as input to a cold-dark-matter simulation code developed by Hu and Miralda-Escudé. This code[30] computes the shear power spectrum and correlation function for any given cosmology, using the prescription of refs 31 and 32. From this, the mass power spectrum is calculated in the nonlinear regime when the growth of dark-matter structures which have gravitationally collapsed, has modified the mass spectrum. Results were obtained for three cosmological models, and are plotted along with our seeing-corrected measurements on a logarithmic scale in Fig. 5. Two current models were normalized to the microwave background fluctuations (COBE) at large angle and to local galaxy cluster abundance (assuming that mass traces light) at small angle: an open universe with $\Omega_{\mathrm{matter}} = 0.45$ (orange in Fig. 5), and a flat universe dominated by a cosmological constant $\Lambda = 0.67$ (green, solid line). The agreement between the data and the two viable cosmological models is impressive for a first measurement. For comparison purposes we also show the old standard cold dark matter flat cosmology (blue), which is only normalized to COBE. (A full listing of the parameters used in these models is shown in Table 1.) To illustrate the effect of varying $N(z)$, we also plot the Λ-dominated cosmology with $z_0 = 0.3$ (green, dotted line). Since our modelled $N(z)$ peaks at $z = 2z_0$, this lowers the typical redshift from 1.0 to 0.6. Decreasing z_0 decreases the amplitude of the correlations, but has little effect on their shapes. The uncertainty in $N(z)$ implies a factor of several uncertainty in the amplitude of the correlation, and is by far the dominant calibration error.

Despite this uncertainty, standard cold dark matter normalized to COBE is ruled out by the measured values of ξ_1. Although this is not surprising, it is the first (to our knowledge) cosmological constraint from wide-field weak lensing and it agrees with several other methods which disfavour this model[33,34]. The other two models are consistent with the data at the 3σ level. This indication of a low-Ω_{matter} universe here is in agreement with a remarkable array of independent methods, including type Ia supernovae, cosmic microwave background anisotropies, cluster baryon fraction together with cluster mass (lensing) and primaeval deuterium, and the age of the oldest stars coupled with the Hubble constant[35]. However, the shape of ξ_2 is not a good fit to either of these two model cosmologies, which are based on a single power-law mass spectrum.
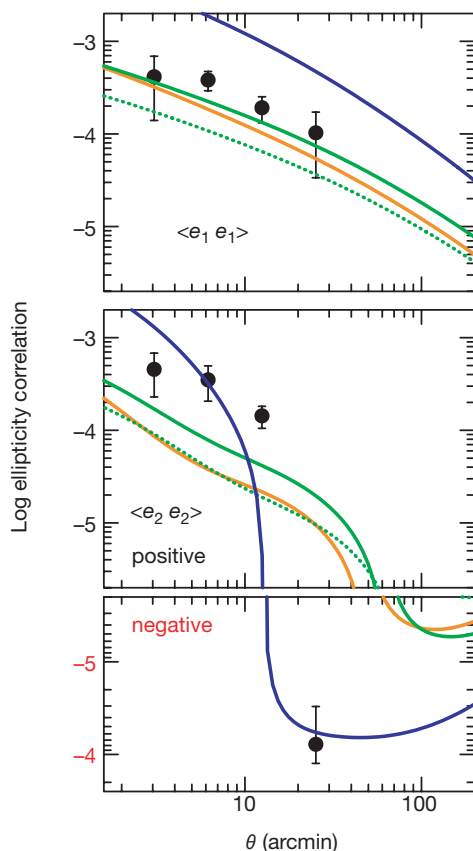
If confirmed by further data, this would suggest the need for a more complicated mass spectrum.

This technique can further distinguish between open and Λ-dominated universes if extended to the somewhat larger angular scales where those cosmologies predict ξ_2 will cross zero as shown in Fig. 5. A survey of many $2° \times 2°$ fields now underway will rule out one or more of these cosmologies at the $\sim 8\sigma$ level at 10-arcmin angles (3σ level for a differential measure of the slope of the power spectrum). Separating the background galaxies into discrete redshift bins based on multi-colour photometry will enable measurement of the ellipticity correlation (or equivalently the dark-matter power spectrum) as a function of cosmic time; wide-field weak lensing surveys deep enough to identify galaxies at $z\sim2$ and measure their shapes will constrain several cosmological parameters[30]. Ultimately, the combination of all the power-spectrum probes (lensing, cosmic microwave background, galaxy distributions, and peculiar velocities) will tightly constrain theories of the origins of fluctuations in the early Universe and their growth into galaxies and large-scale structure. □

1. Page, L. & Wilkinson, D. T. The cosmic microwave background. *Rev. Mod. Phys.* **71,** 173–179 (1999).
2. Tyson, J. A., Valdes, F. & Wenk, R. Detection of systematic gravitational lens galaxy image alignments: mapping dark matter in galaxy clusters. *Astrophys. J.* **349,** L1–L4 (1990).
3. Fahlman, G., Kaiser, N., Squires, G. & Woods, D. Dark matter in MS1224 from distortion of background galaxies. *Astrophys. J.* **437** 56–62 (1994).
4. Squires, G., Kaiser, N., Fahlman, G., Babul, A. & Woods, D. A weak gravitational lensing analysis of Abel 2390. *Astrohys. J.* **469,** 73–77 (1996).
5. Clowe, D., Luppino, G. A., Kaiser, N., Henry, J. P. & Gioia, I. M. Weak lensing by two $z \sim 0.8$ clusters of galaxies. *Astrophys. J.* **497** 61–64 (1998).
6. Hoekstra, H., Franx, M., Kuijken, K. & Squires, G. Weak lensing analysis of CL 1358+62 using hubble space telescope observations. *Astrophys. J.* **504,** 636–660 (1998).
7. Mellier, Y. Probing the universe with weak lensing. *Annu. Rev. Astron. Astrophys.* **37,** 127–189 (1999).
8. Gunn, J. E. A fundamental limitation on the accuracy of angular measurement in observational cosmology. *Astrophys. J.* **147,** 61–72 (1967).
9. Dyer, C. & Roeder, R. Observations in locally inhomogeneous cosmological models. *Astrophys. J.* **189,** 167–175 (1974).
10. Miralda-Escudé, J. The correlation function of galaxy ellipticities produced by gravitational lensing. *Astrophys. J.* **380,** 1–8 (1991).
11. Blandford, R., Saust, A., Brainerd, T. & Villumsen, J. The distortion of distant galaxy images by large scale structure. *Mon. Not. R. Astron. Soc.* **251,** 600–627 (1991).
12. Kaiser, N. Weak gravitational lensing of distant galaxies. *Astrophys. J.* **388,** 272–286 (1992).
13. Villumsen, J. Weak lensing by large-scale structure in open, flat and closed universes. *Mon. Not. R. Astron. Soc.* **281,** 369–383 (1996).
14. Jain, B. & Seljak, U. Cosmological model predictions for weak lensing. *Astrophys. J.* **484,** 560–573 (1997).
15. Kaiser, N. Weak lensing and cosmology. *Astrophys. J.* **498,** 26–42 (1998).
16. Kristian, J. On the cosmological distortion effect. *Astrophys. J.* **147,** 864–867 (1967).
17. Valdes, F., Tyson, J. A. & Jarvis, J. F. Alignment of faint galaxy images: cosmological distortion and rotation. *Astrophys. J.* **271,** 431–441 (1983).
18. Mould, J. *et al.* A search for weak distortions of distant galaxy images by large-scale structure. *Mon. Not. R. Astron. Soc.* **271,** 31–38 (1994).
19. Schneider, P. *et al.* Detection of shear due to weak lensing by large-scale structure. *Astron. Astrophys.* **333,** 767–778 (1998).
20. Wittman, D. *et al.* Big SPIE throughput camera: the first year. *Proc. SPIE* **3355,** 626–634 (1998).
21. Castleman, K. R. *Digital Image Processing* 214 (Prentice Hall, Englewood Cliffs, New Jersey, 1979).
22. Fischer, P. & Tyson, J. A. The mass distribution of the most luminous x-ray cluster RXJ1347.5-1145 from gravitational lensing. *Astron. J.* **114,** 14–24 (1997).
23. Gullixson, C. A., Boeshaar, P. C., Tyson, J. A. & Seitzer, P. The $B_j RI$ photometric system. *Astrophys. J. Suppl. Ser.* **99,** 281–293 (1995).
24. Bertin, E. & Arnouts, S. Sextractor: software for source extraction. *Astron. Astrophys. Supp.* **117,** 393–404 (1996).
25. Valdes, F. Resolution classifier. *Proc. SPIE* **331,** 465–472 (1982).
26. Tyson, J. A. in *AIP Conf. Proc. Dark Matter* (eds Holt, S. & Bennett, C.) 287–296 (AIP Press, 1995).
27. Wittman, D. & Tyson, J. A. The shear correlation function out to 20 arcminutes. In *Gravitational Lensing: Recent Progress and Future Goals* (eds Brainerd, T. G. & Kochanek, C. S.) (ASP Conference Series, Astronomical Society of the Pacific, San Francisco, in the press).
28. Kruse, G. & Schneider, P. The non-gaussian tail of cosmic shear statistics. Preprint astro-ph/9904192 at ⟨http://xxx.lanl.gov⟩ (1999).
29. Tran, K. H. *et al.* The velocity dispersion of MS1054-03: a massive galaxy cluster at high redshift. *Astrophys. J.* **522,** 39–45 (1999).
30. Hu, W. Power spectrum tomography with weak lensing. *Astrophys. J.* **522,** L21–L24 (1999).
31. Hamilton, A. J. S., Matthews, A., Kumar, P. & Lu, E. Reconstructing the primordial spectrum of fluctuations of the universe from the observed nonlinear clustering of galaxies. *Astrophys. J.* **374,** L1–L4 (1991).
32. Peacock, J. A. & Dodds, S. J. Non-linear evolution of cosmological power spectra. *Mon. Not. R. Astron. Soc.* **280,** L19–L26 (1996).
33. Ostriker, J. P. & Steinhardt, P. J. The observational case for a low density universe with a cosmological constant. *Nature* **377,** 600–602 (1995).
34. Bahcall, N. A., Ostriker, J. P., Perlmutter, S. & Steinhardt, P. J. The cosmic triangle: revealing the state of the universe. *Science* **284,** 1481–1488 (1999).
35. Turner, M. S. & Tyson, J. A. Cosmology at the millennium. *Rev. Mod. Phys.* **71,** 145–164 (1999).
36. Frenk, C., White, S. D. M., Efstathiou, G. & Davis, M. Galaxy clusters and the amplitude of primordial fluctuations. *Astrophys. J.* **351,** 10–21 (1990).